Int J Adv Manuf Technol (2017) 90:2263–2270
DOI 10.1007/s00170-016-9501-8

ORIGINAL ARTICLE

Laser beam welding of 316L T-joint: microstructure, microhardness, distortion, and residual stress

Youmin Rong[1] · **Yu Huang**[1] · **Guojun Zhang**[1] · **Gaoyang Mi**[2] · **Wenjun Shao**[1]

Received: 12 May 2016 / Accepted: 16 September 2016 / Published online: 13 October 2016

Abstract Austenitic stainless steel 316L is welded by laser beam with T-joint in this paper. Microstructures of fusion zone consist of a large amount of austenite and a small amount of ferrite; heat-affected zone (HAZ) width is about 10 μm. The fine-equiaxed dendrites existing as network morphology locate at the center of fusion zone, and columnar structures are near HAZ. Microhardness at the top of the cross-section of welded joints is higher than that at the bottom, and the hardness of the second pass is higher than that of the first pass. The numerical result of maximum deformation (2.67 mm) keeps a good line with that of the experiment result (2.52 mm). The maximum value of the longitudinal compressive stress is 306 MPa, while the residual stress of the first pass is slightly released during the second pass welding process. The transverse residual stress along line 1 always presents a compressive state. At the 3.5 mm position far from the bead center, a large fluctuation of angular deformation and longitudinal residual stress are induced by the high-temperature gradient. Maximum values of angular deformation and equivalent residual stress for the whole sample are 1.37 mm and 452.3 MPa, and these both locate at the end-start zone of the welding path.

✉ Gaoyang Mi
hustmigaoyang@163.com

Youmin Rong
ymrong1987@gmail.com

[1] State Key Lab of Digital Manufacturing Equipment and Technology, School of Mechanical Science and Engineering, Huazhong University of Science and Technology, Wuhan, China

[2] School of Material Science and Engineering, Huazhong University of Science and Technology, Wuhan, China

Keywords Laser welding · Microstructure · Microhardness · Distortion · Residual stress · 316L

1 Introduction

Stainless steel has been widely exploited in a range of industry applications with its advantages of corrosion resistant and long lasting, making thinner and more durable structure possible [1]. Generally, stainless steel structures are joined by welding process [2], and it is necessary to investigate its welding performance from the point of microstructure and mechanical properties.

Recently, microstructure of stainless steel obtained by welding process has been researched. The relationship from welding parameters and external environment to microstructure is mostly concerned. Kumar and Shahi revealed the influence from welding parameters (current, voltage, and welding speed) on microstructural changes [3]. To investigate the effect of tungsten inert gas process on delta ferrite content of 316L steel, five kinds of oxide fluxes, including MnO_2, TiO_2, MoO_3, SiO_2, and Al_2O_3, are considered by Tseng and Hsu [4]. Cho et al. demonstrated that the significant microstructure changes are caused by severe deformation and the high heat input during friction stir welding (FSW) 409 steel [5]. It was confirmed by Bang et al. that re-crystallization in FSW was induced by preheating, and thus, the grain size and dislocation density were both decreased [6]. Mukherjee proved that grain structure and direction of grain growth in low nickel austenitic stainless steel weld metals can be affected by different modes of metal transfer (short circuit mode, spray mode, and pulse mode) [7].

Meanwhile, mechanical properties of welding joints, including welding deformation, residual stress, tensile strength, fracture, and so on, have got much attention. The influences of

different restraints on the welding deformation and residual stress were researched by Adak and Soares [8]. Ravisankar et al. applied simulation and experiment methods to research the influence of welding speed and power on residual stress [9]. Elmesalamy et al. compared laser welding and arc welding residual stresses in multi-pass narrow gap [10]. Ye et al. investigated the relationship between different groove types with residual stress and welded-induced deformation [11]. Alipooramirabad et al. explained the distribution of residual stress in multi-pass welding using neutron diffraction [12]. Microhardness of AISI 420 butt joint obtained by laser welding was measured by Erdem et al. [13]. Alizadeh-Sh et al. found that the welding cycle has an obvious effect on the mechanical properties in terms of peak load, energy absorption, and failure mode [14]. The improvement method of tensile and impact strength was discussed by appropriate filler without obtaining any deleterious phases [15]. The fatigue life and fatigue crack growth of friction stir-welded AISI 409M stainless steel joints were evaluated using hourglass and central-cracked tension specimens, respectively [16].

According to the previous work, there are three characteristics of the welding process of stainless steel can be concluded that the primary attention of each article concentrates separately on one aspect of microstructure or mechanical properties; the joining type is mainly butt joint; welding method is mostly arc welding. It is noted that T-joint is widely applicable especially for large-scale structures. However, there is no related research about microstructure and mechanical properties of a same T-joint obtained by laser welding. Therefore, a case of laser welding 316L steel with T-joint is focused in this paper, while microstructure, microhardness, distortion, and residual stress are all further discussed.

2 Experiment

Base metal is austenite steel 316L, and its chemical components are given in Table 1 [17]. The diagram of the sample with T-joint is shown in Fig. 1. The flange and web plate are welded into T-joint with the size of both 100 × 100 × 5 mm, while the measurement position of angular distortion and residual stress is noted as line 1. To ensure the welding quality, each contact zone of the plates is flatted by grinding process and then cleaned by acetone before welding. Figure 2 gives

Table 1 Chemical components of austenite steel 316L (wt.%)

C	Si	Mn	P	S	Cr	Mo	Ni	N	Cu
0.021	0.77	1.019	0.039	0.001	16.92	2.03	12.16	0.033	0.20

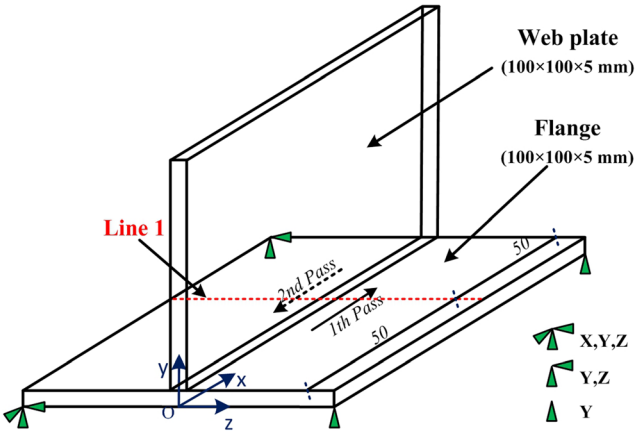

Fig. 1 Diagram of 316L sample with T-joint

the laser welding system. The whole welding process is completed using teaching method. The sample is clamped by the jig and inclined about 45° so that the laser beam can reach the welded zone. Detailed welding parameters are listed as follows: fiber laser power is 4 KW, welding speed is 0.6 m/min, shielding gas is Ar with flux of 0.6 m^3/h, and cooling time between two passes is 240 s.

3 Microstructure and microhardness

3.1 Measurement methods

To observe microstructure and measure microhardness, the welded sample is cut by wire-cut electrical discharge

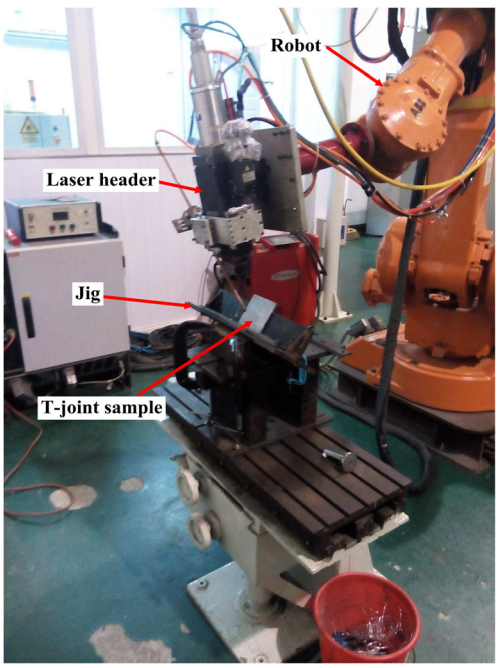

Fig. 2 Laser welding system

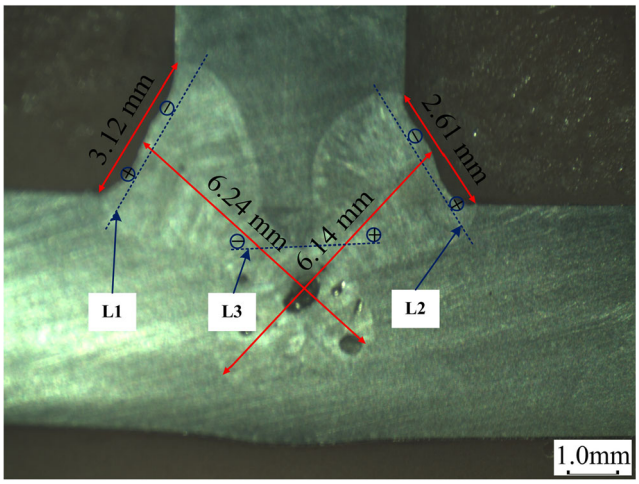

Fig. 3 Bead geometry of 316L steel with T-joint

machining, and then the sample is eroded by the aqua regia with the purity of 100 %. The optical microscope with different magnification (10, 100, 200, and 500) times is used to extract the image of the bead geometry and further observe the microstructure. Meanwhile, microhardness of welded zone is measured with load 300 g and hold-up time 15 s. As shown in Fig. 3, measurement positions of hardness are noted by three blue lines (L1, L2, and L3), while intermediate position of each measuring line is recorded as zero so that measurement results can be easy expressed using different curves.

3.2 Microstructure

The bead geometry is shown in Fig. 3. The first and second passes are distributed in both left and right sides. It is apparent that some obvious porosities near the cross position of two welding passes may be caused by slags or re-solidification. Widths of the first and second seam are 3.12 and 2.61 mm, while penetrations are 6.24 and 6.14 mm in turn. It can be concluded that the first pass in bead profile keeps high consistent with the second pass. The microstructure of base metal 316L is austenite (Fig. 4a). The dendrite growth direction in the seam center (Fig. 4b) is clearly different, while the angle between two growth directions is about 120°. This is decided by flow of weld pool and temperature gradient. As shown in Fig. 4c and d, microstructures of the seam zone consist of a large amount of austenite and a small amount of ferrite. The interface zone between base metal and fusion zone is analyzed in Fig. 5. It is obvious that the heat-affected zone (HAZ) is very small (about 10 μm) because of solidification of the weld metal at higher cooling rates. Compared Fig. 4 with Fig. 5, it can be found that the growth direction of columnar dendrites is from the interface to the center of the molten pool, while the finest-equiaxed dendrites existing as network morphology in the center of fusion zone. Generally, the primary dendrite arm spacing of columnar structure is mainly affected by the cooling rate and the heat input. In other words, the higher cooling rate and the lower heat input tend to refine the primary dendrite arm spacing [18]. The distribution of these solidification microstructures in fusion zone is induced by the thermal gradient (G) and the

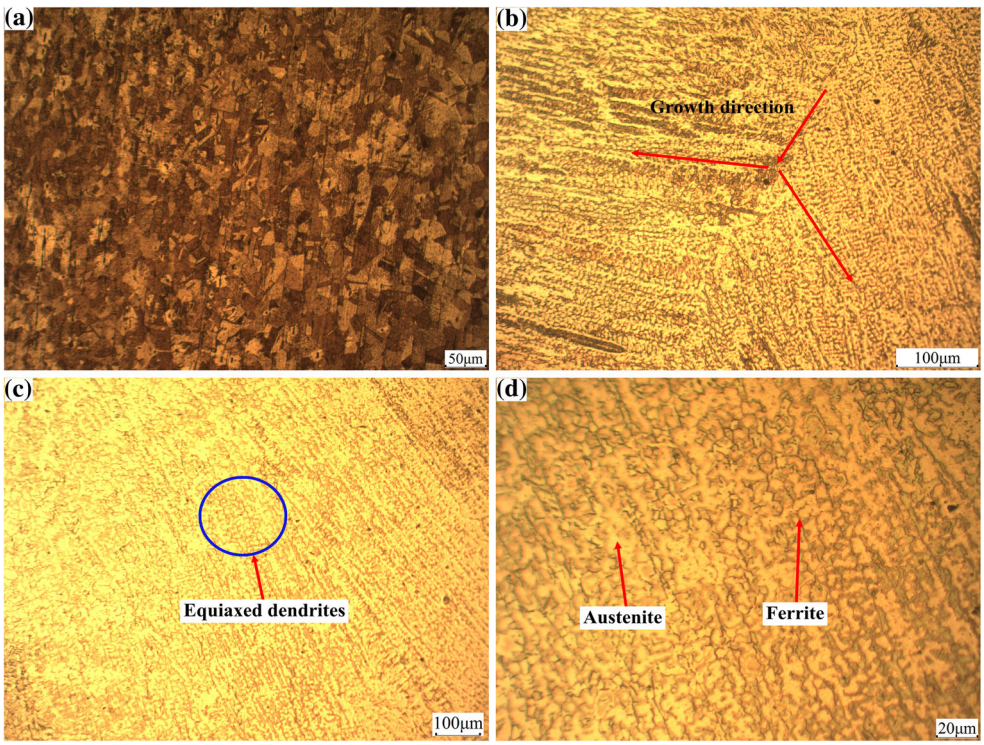

Fig. 4 Microstructures of **a** base metal, **b** center of right seam, and **c** weld zone magnified 100 times and **d** 500 times

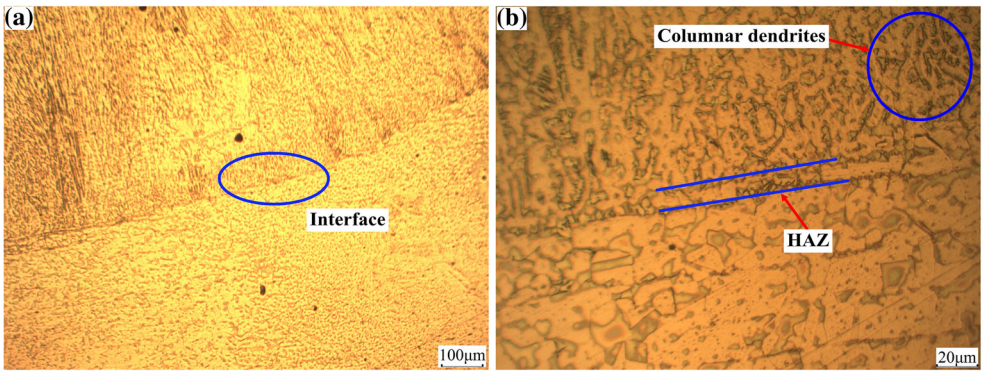

Fig. 5 Interface zone with magnification of **a** 100 times and **b** 500 times

cooling rate (R) [19, 20]. The fine dendritic structure is produced mainly by rapid R in fiber laser welding, while the columnar dendrites grows much easier with a higher ratio of thermal gradient to cooling rate (G/R). Meanwhile, the microstructure of the cross zone between the first pass and second pass is given in Fig. 6. Compared with the first pass, the columnar dendrite is much more clear and larger, while its size tends smaller with a closer distance from the first pass. HAZ of second pass is also more obvious than that of the first pass. It is found that this phenomenon at cross zone might be caused by the second thermal cycle and the re-solidification.

3.3 Microhardness

The measurement results of the microhardness for two weld seams and their cross zone are given in Fig. 7. The fluctuation tendency of the measurement results of the first pass is similar to that of the second pass. The microhardness of the weld beam is higher than that of the base metal 316L. As it gets closer to the center, the microhardness abruptly increases and the highest values of L1 and L2 are 215.8 and 249.2 HV. At the same time, it can be found that the high hardness values appear in the finest-equiaxed dendrites zone, because this appearance is related to the grain size and the content of alloy elements. Meanwhile, the value of the second pass (L2) is generally higher than that of the first pass (L1), and this phenomenon can be explained by that the first pass is equivalent to be heat treated while the second beam is formed by laser welding. Compared the hardness values of L1, L2, and L3, it is noted that the microhardness at the top of the cross-section of the welded joint is higher than that at the bottom [20]. The distribution of microhardness near the cross zone (L3) is similar to that of L1 and L2, and the only difference is the size of the measured values.

4 Welding deformation and residual stress

4.1 Measurement methods

For 316L steel sample with T-joint, Fig. 8 shows the measurement method of the angular distortion. Compared with the actual angular deformation for each side of the flange plate, the cock height of the another side is proximately double times than the actual distortion after that one side of flange plate is pressed on the cast iron platform. It is noted that the cock height is measured by vernier caliper with the accuracy of 0.02 mm. Meanwhile, the distance between each measurement point is 10.0 mm.

4.2 Finite element theory of thermal elastic–plastic method

To further reveal the mechanical properties of 316L T-joint, welding deformation and residual stress are researched by

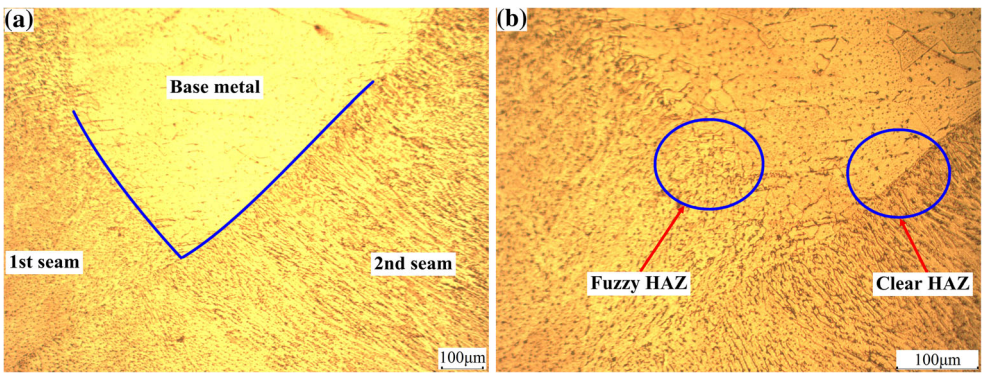

Fig. 6 Cross area of two passes with magnification of **a** 100 times and **b** 200 times

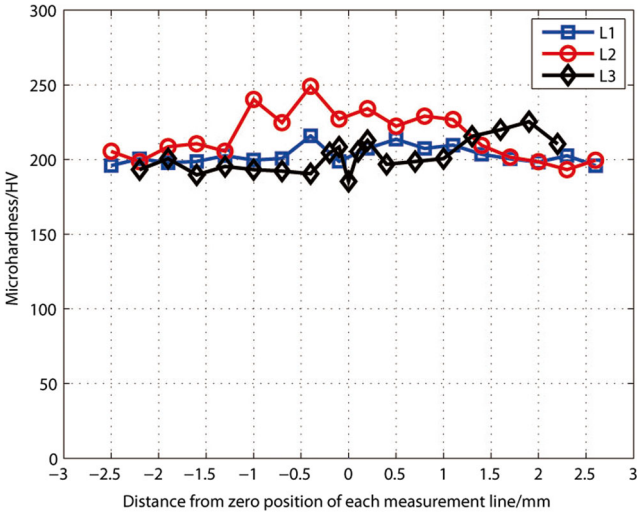

Fig. 7 Microhardness curves of three measurement lines (L1, L2, and L3) noted in Fig. 3

thermal elastic–plastic finite element model (TEP-FEM) and experiment validation. TEP-FEM is developed by ANSYS parametric design language (APDL). The full 3D geometry (Fig. 1) is built within the framework of numerical investigations. To discretize 3D geometry, eight-node SOLID70 elements are used for the thermal analysis, and SOLID185 elements are applied for the mechanical analysis. The 3D mesh consists of 100,500 elements, while the amounts of DOF of each node for thermal and mechanical analysis are 1 and 3, respectively.

In the thermal analysis, the finite element formulation for the transient nonlinear heat transfer is governed by Eq. (1).

$$\rho c_p \frac{\partial T}{\partial t} = \frac{\partial}{\partial x}\left(\lambda \frac{\partial T}{\partial x}\right) + \frac{\partial}{\partial y}\left(\lambda \frac{\partial T}{\partial y}\right) + \frac{\partial}{\partial z}\left(\lambda \frac{\partial T}{\partial z}\right) + Q_L \quad (1)$$

Fig. 8 Measurement method of angular distortion

Table 2 Constants of Goldak's model

Symbol	Value	Symbol	Value
η	80 %	b	6.0 mm
P_L	4000 W	c	1.6 mm
a_f	3.0 mm	f_f	0.545
a_r	8.0 mm	f_r	1.455

where ρ represents density, λ is thermal conductivity, c_p expresses specific heat capacity, and Goldak's heat source Q_L model can be calculated by Eqs. (2)–(4) [21].

$$Q_L = q_f + q_r, \quad (2)$$

$$q_f = \frac{6\sqrt{3} f_f \eta P_L}{a_f bc\pi\sqrt{\pi}} e^{-3x^2/a_f^2} e^{-3y^2/b^2} e^{-3z^2/c^2} \quad x \geq 0, \quad (3)$$

$$q_r = \frac{6\sqrt{3} f_r \eta P_L}{a_r bc\pi\sqrt{\pi}} e^{-3x^2/a_r^2} e^{-3y^2/b^2} e^{-3z^2/c^2} \quad x < 0, \quad (4)$$

where η is efficiency of heat source, and P_L is laser power. Geometrical parameters of heat source model are a_f, a_r, b and c. Note that $f_f + f_r = 2$. Constants of the heat source model are listed in Table 2. Movement of the heat source in numerical process is simulated by moving origin position of the local coordinate system. Meanwhile, *xoy* plane in local coordinate system is perpendicular with weld width direction. In Eqs. (3) and (4), x direction parallels with welding direction, y direction means welding penetration, and z direction presents bead width. The thermal material properties depending on temperature [22] are shown in Fig. 9. During welding process, it is necessary to consider the influence from the heat losses because of the heat convection and radiation. By converting radiation

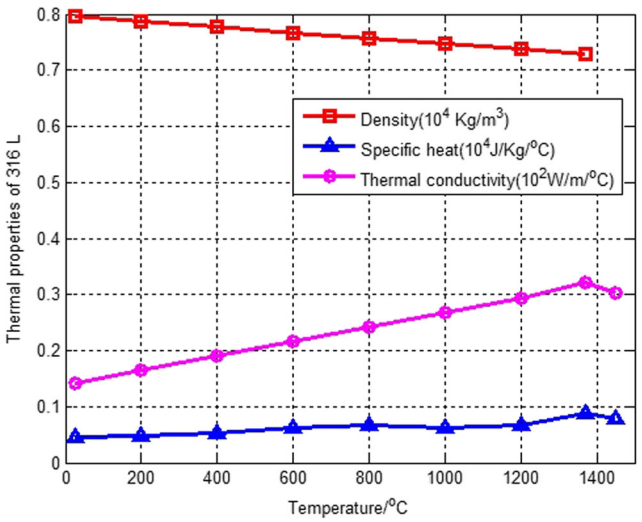

Fig. 9 Thermal properties of 316L steel

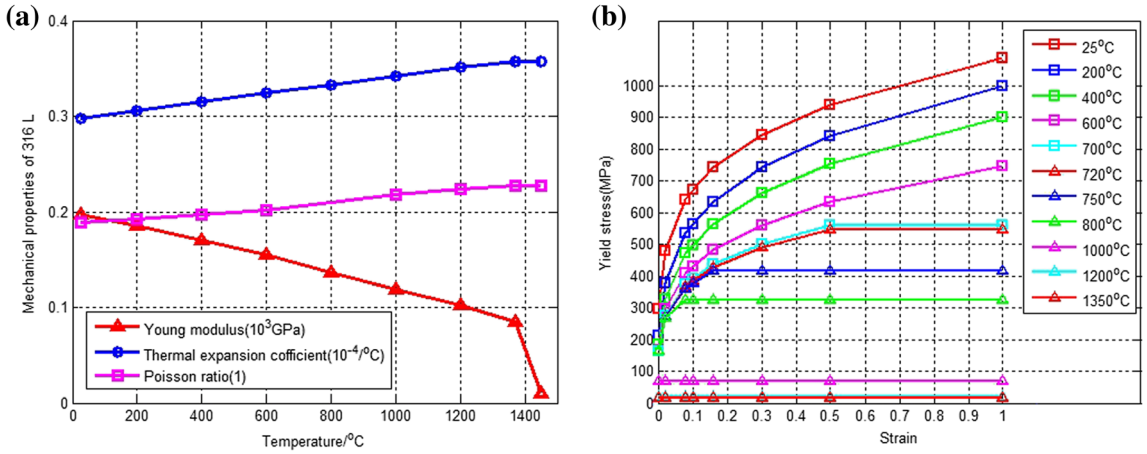

Fig. 10 Mechanical properties of 316L. **a** Young modulus, thermal expansion coefficient and Poisson's ratio, and **b** yield stress with different strain and temperature

as a part of the convection, the total thermal convection coefficient h_c (W/($m^2 \cdot {}^oC$)) is given as Eq. (5) [23].

$$h_c = \begin{cases} 0.0668T & W/\left(m^2 \cdot {}^oC\right) \quad T < 500^oC \\ 0.231T - 82.1 & W/\left(m^2 \cdot {}^oC\right) \quad T \geq 500^oC \end{cases} . \tag{5}$$

In mechanical analysis stage, four constraints are distributed in the four corner points as shown in Fig. 1 to avoid the rigid displacement in computation process, while the temperature-dependent mechanical properties of 316L steel [22] are presented in Fig. 10. The material is modeled as an elastic–plastic solid with kinematic hardening. Nonlinear material behavior is developed by increasing plasticity with the von Mises yield criterion together with the associated flow rule and assuming geometrically nonlinear behavior of the two plates [24]. Meanwhile, Newton–Raphson solution technique is applied to update stresses.

4.3 Results and discussion

Comparison analysis of bead profile along line 1 (Fig. 1) between the numerical result and the experiment result is given in Fig. 11a. The simulation result of bead shape is similar to the experiment result, except that large error of bead geometry between computation and experiment results appears in the seam root zone. This large error is caused by heat source model and thermal conductivity of high temperature. Figure 11b shows the temperature field at 270 s after the beginning of the laser welding process, and the highest temperature is 631.3 °C.

Angular distortion and residual stress are drawn in Fig. 12. As shown in Fig. 12a, the maximum deformations of simulation and experiment results are 2.67 and 2.52 mm, and further relative error [25] is −5.95 %. It is obvious that numerical results keep a good line with the experiment measurement results. According to simulation

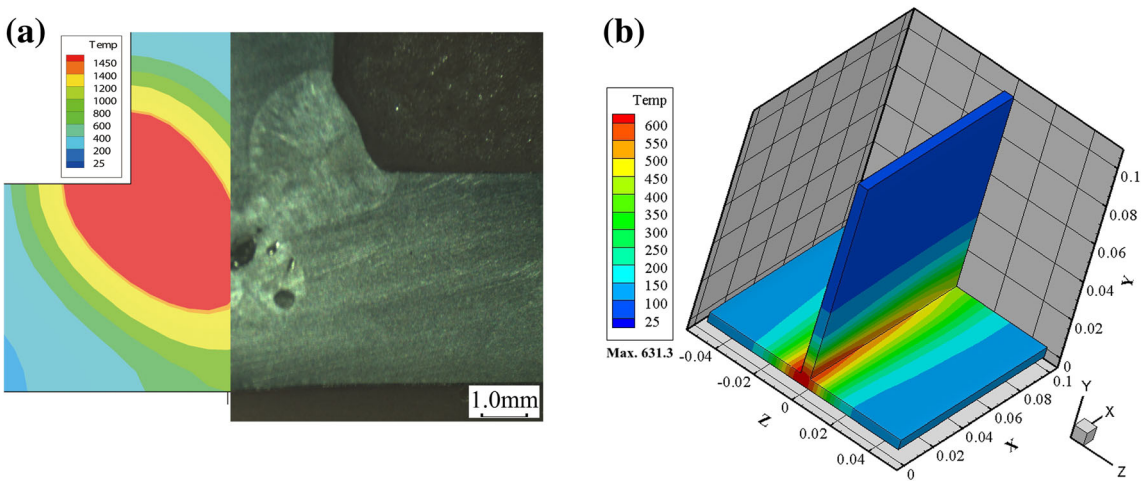

Fig. 11 Finite element analysis results of **a** bead geometry along line 1 and **b** temperature field 270 s after the beginning of the welding process

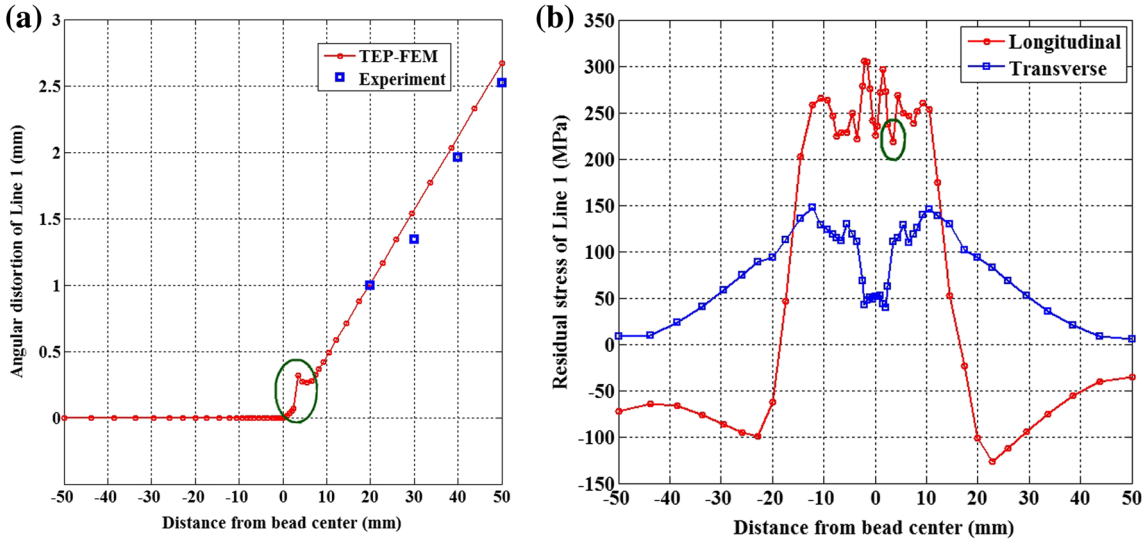

Fig. 12 Simulation results of **a** angular distortion and experiment validation, and **b** residual stress along line 1

results in Fig. 12b, the maximum value of the longitudinal compressive stress is 306 MPa which occurs in the second pass, while that is 296 MPa in the first pass. It is hinted that residual stress of first pass is slightly released during the second pass welding process. The maximum value of longitudinal tension stress is 126.9 MPa, and this appears at 22.8 mm position. Meanwhile, the transverse residual stress along Line 1 always presents a compressive state, and the tendency is more intense near the seam zone. At the 3.5 mm position far from the bead center, there is a large fluctuation of angular deformation and longitudinal residual stress. This phenomenon may be caused by the high-temperature gradient. The maximum value of angular deformation for the whole sample is 1.37 mm (Fig. 13a), and its position locates at the end and start areas of the welded seam. The distribution of von Mises equivalent residual stress is given in Fig. 13b, and its peak value located near the end-start position of welding path is 452.3 MPa.

5 Conclusions

T-joint of stainless steel 316L is the basis of large-scale structures, but there is no related research about microstructure and mechanical properties of a same T-joint. Therefore, microstructure, microhardness, deformation, and residual stress are all discussed in this paper.

The following conclusions are drawn based on experiment and numerical results:

(1) Microstructures of fusion zone consist of a large amount of austenite and a small amount of ferrite, and HAZ is very small (about 10 μm) because of solidification of the weld metal at higher cooling rates. The dendrite growth direction in the seam center is clearly different, while the angle between two growth directions is about 120°.

(2) The microhardness at the top of the cross-section of the welded joint is higher than that at the bottom, and the hardness of the second pass is higher than that of the first

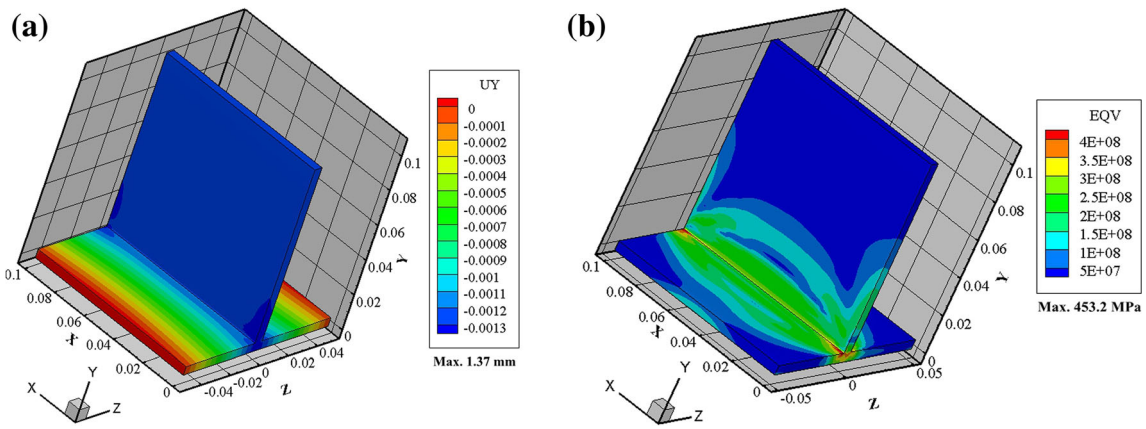

Fig. 13 Distribution for the whole T-joint sample of **a** angular distortion and **b** von Mises stress

pass because of the equivalent heat treated in the second laser welding process. The fine-equiaxed dendrites existing as network morphology in the center of fusion zone has higher hardness than that of the columnar structures near HAZ.

(3) The maximum deformations of simulation and experiment results are 2.67 and 2.52 mm, and further relative error is −5.95 %. The numerical results keep a good line with the experiment measurement results. The maximum value of the longitudinal compressive stress is 306 MPa, while the residual stress of the first pass is slightly released during the second pass welding process.

(4) The transverse residual stress along line 1 always presents a compressive state, and the high-temperature gradient induces a large fluctuation of angular deformation and longitudinal residual stress at the 3.5-mm position far from the bead center. Meanwhile, the maximum values of angular deformation and von Mises equivalent residual stress for the whole sample are 1.37 mm and 452.3 MPa, and these both locate at the end-start zone of the welding path.

Acknowledgments This research is supported by the National Basic Research Program of China (973 Program, No. 2014CB046703) and the Fundamental Research Funds for the Central Universities (HUST: 2016YXMS271). The authors also express their gratitude to engineer Xiyuan Hu and master Zeyang Zhao for their help in experiment operation.

References

1. Baddoo NR (2008) Stainless steel in construction: a review of research, applications, challenges and opportunities. J Constr Steel Res 64:1199–1206
2. Gardner L (2005) The use of stainless steel in structures. Prog Struct Engng Mater 7:45–55
3. Kumar S, Shahi AS (2014) On the influence of welding stainless steel on microstructural development and mechanical performance. Mater Manuf Process 29:894–902
4. Tseng KH, Hsu CY (2011) Performance of activated TIG process in austenitic stainless steel welds. J Mater Process Technol 211:503–512
5. Cho HH, Hong ST, Roh JH, Choi HS, Kang SH, Steel RJ, Han HN (2013) Three-dimensional numerical and experimental investigation on friction stir welding processes of ferritic stainless steel. Acta Mater 612:649–2661
6. Bang HS, Bang HS, Jeon GH, Oh IH, Ro CS (2012) Gas tungsten arc welding assisted hybrid friction stir welding of dissimilar materials Al6061-T6 aluminum alloy and STS304 stainless steel. Mater Des 37:48–55
7. Mukherjee M, Saha S, Pal TK, Kanjilal P (2015) Influence of modes of metal transfer on grain structure and direction of grain growth in low nickel austenitic stainless steel weld metals. Mater Charact 102:9–18
8. Adak M, Soares CG (2014) Effects of different restraints on the weld-induced residual deformations and stresses in a steel plate. Int J Adv Manuf Technol 71:699–710
9. Ravisankar A, Velaga SK, Rajput G, Venugopal S (2014) Influence of welding speed and power on residual stress during gas tungsten arc welding (GTAW) of thin sections with constant heat input: a study using numerical simulation and experimental validation. J Manuf Process 16:200–211
10. Elmesalamy A, Francis JA, Li L (2014) A comparison of residual stresses in multi pass narrow gap laser welds and gas-tung sten arc welds in AISI 316L stainless steel. Int J Pressure Vessels Pip 113: 49–59
11. Ye YH, Cai JP, Jiang XH, Dai DP, Deng DA (2015) Influence of groove type on welding-induced residual stress, deformation and width of sensitization region in a SUS304 steel butt welded joint. Adv Eng Softw 86:39–48
12. Alipooramirabad H, Paradowska A, Ghomashchi R, Kotousov A, Reid M (2015) Quantification of residual stresses in multi-pass welds using neutron diffraction. J Mater Process Technol 226:40–49
13. Erdem M, Altug M, Karabulut M (2016) Investigation of mechanical, microstructural, and machining properties of AISI 420 martensitic stainless steel welded by laser welding. Int J Adv Manuf Technol 85:481–492
14. Alizadeh-Sh M, Marashi SPH, Pouranvari M (2014) Resistance spot welding of AISI 430 ferritic stainless steel: phase transformations and mechanical properties. Mater Des 56:258–263
15. Devendranath Ramkumar K, Thiruvengatam G, Sudharsan SP, Mishra D, Arivazhagan N, Sridhar R (2014) Characterization of weld strength and impact toughness in the multi-pass welding of super-duplex stainless steel UNS 32750. Mater Des 60:125–135
16. Lakshminarayanan AK, Balasubramanian V (2012) Assessment of fatigue life and crack growth resistance of friction stir welded AISI 409M ferritic stainless steel joints. Mater Sci Eng A-Struct Mater Prop Microstruct Process 539:143–153
17. Feng YQ, Luo Z, Liu ZM, Li Y, Luo YC, Huang YX (2015) Keyhole gas tungsten arc welding of AISI 316L stainless steel. Mater Des 85:24–31
18. Lee HT, Jeng SL, Yen CH, Kuo TY (2004) Dissimilar welding of nickel-based alloy 690 to SUS 304L with Ti addition. J Nucl Mater 335:59–69
19. Janaki Rama GD, Venugopal Reddy A, Prasad Rao K, Reddy GM, Sarin Sundar JK (2005) Microstructure and tensile properties of Inconel 718 pulsed Nd-YAG laser welds. J Mater Process Technol 167:73–82
20. Cui CY, Cui XG, Ren XD, Liu TT, Hu JD, Wang YM (2013) Microstructure and microhardness of fiber laser butt welded joint of stainless steel plates. Mater Des 49:761–765
21. Goldak J, Chakravarti A, Bibby M (1984) A new finite element model for welding heat sources. Metall Trans B 15:299–305
22. Rong YM, Zhang GJ, Huang Y (2016) Study on deformation and residual stress of laser welding 316L T-joint using 3D/shell finite element analysis and experiment verification. Int J Adv Manuf Technol. doi:10.1007/s00170-016-9246-4
23. Brickstad B, Josefson BL (1998) A parametric study of residual stresses in multi-pass butt-welded stainless steel pipes. Int J Pressure Vessels Pip 75:11–25
24. Benedetti M, Fontanari V, Santus C (2013) Crack growth resistance of MAG butt-welded joints of S355JR construction steel. Eng Fract Mech 108:305–315
25. Rong YM, Zhou Q, Huang Y, Chang Y, Zhang GJ, Shao XY (2016) Multi-objective optimization of laser brazing with the crimping joint using ANN and NSGA-II. Int J Adv Manuf Technol 85: 1239–1247